Post-processing of large-eddy simulations for jet noise predictions

By S. Mendez, M. Shoeybi, A. Sharma, S. K. Lele AND P. Moin

1. Motivation and objectives

Despite almost 60 years of active research on jet noise, the noise generated by expulsion of hot gases at the exhaust of aircraft engines remains an important part of the total aircraft noise. This is particularly true in the case of supersonic aircrafts, where the high speed of the exhaust gases yields extremely high noise. In the framework of the development of future civil supersonic aircrafts, it is of major importance to decrease the noise from supersonic jets in order to comply with strict noise regulations enforced in civil air transportation.

To assist the experimental efforts in finding innovative solutions for jet noise reduction, numerical methods have been developed. Among them, Large-Eddy Simulation (LES) has the potential to become a tool of choice to perform predictions of the noise generated by turbulent jets (Bodony & Lele 2008). It does not have the same limitation in Reynolds number as Direct Numerical Simulation and thus can handle cases relevant to industrial applications. From the physical point of view, LES is well adapted to jet noise computations, because important contribution to jet noise comes from the large scales of the turbulent flow (Tam 1995, 1998; Bogey & Bailly 2006), for which Reynolds-Averaged Navier-Stokes methods fail to provide a good description in the general case.

One of the outputs of interest in jet noise study is the far-field noise. While LES is well suited for the computation of the flow, it would be inefficient to use it to propagate acoustic waves to the far field. In order to compute the far-field noise, one relies on acoustic analogies: volumetric methods such as Lighthill analogy (Lighthill 1952; Freund 2001; Uzun *et al.* 2004) allow modeling of noise sources and computation of the far-field sound. Surface integral methods like Kirchhoff (Farassat & Myers 1988) or Ffowcs-Williams & Hawkings (Ffowcs Williams & Hawkings 1969) methods (with volumetric source terms, corresponding to the presence of quadrupoles outside the surface, neglected) rely on near-field information gathered over a surface enclosing as much as possible the noise sources. The latter methods, owing to their limited cost and their success (coupled with LES) in predicting the noise emitted by high-speed jets, are now very popular in the jet noise LES community.

However, the diversity of results presented in the literature suggests that details of implementation are important, and that a thorough study of the capacity of such methods has to be undertaken, as done by Rahier *et al.* (2003) and Shur, Spalart & Strelets (2005), among others, before using it routinely. To post-process the jet noise results obtained by the compressible version of the unstructured LES solver CDP (Shoeybi *et al.* 2009), a solver using the Ffowcs-Williams & Hawkings (FWH) surface integral method has been implemented. The purpose of this report is to document and analyze far-field acoustic results obtained from a set of LES to determine best practices when using a FWH solver for jet noise predictions.

2. Numerical method

In the present study, we use the frequency domain permeable surface FWH formulation (Ffowcs Williams & Hawkings 1969), already described by Ham *et al.* (2009). In this formulation, the volume integral of the original FWH equation is omitted, which generates errors. One of the challenges is to minimize the errors due to the use of the inexact FWH formulation.

This section describes the procedure employed to calculate the far-field sound. The time history of conservative variables is saved over a given surface S (referred to as FWH surface) at a specified sampling frequency f and for a total time τ. f is associated with the Nyquist Strouhal number $St_{max} = f\,D/2U_j$, where $D = 2R$ is the nozzle diameter at the exit (R the radius) and U_j is the jet velocity at the nozzle exit. τ determines the minimum frequency accessible by this post-processing $St_{min} = D/\tau\,U_j$.

For each surface element of S, the time history of source terms F_1 and F_2 are constructed from the conservative variables using the following expressions:

$$F_1 = \frac{p'\hat{n}_j\hat{r}_j + \rho u_j u_n \hat{r}_j}{c_0 r} + \frac{\rho u_n}{r} \qquad \text{and} \qquad F_2 = \frac{p'\hat{n}_j\hat{r}_j + \rho u_j u_n \hat{r}_j}{r^2}. \tag{2.1}$$

$\hat{n}_j$ is the jth component of the unit surface normal vector, and $r\hat{r}_j$ represents magnitude and direction of the vector from the surface element location $\mathbf{y}$ to the observer location $\mathbf{x}$. In the expression of F_1 and F_2, p' is the fluctuating pressure ($p' = p - p_\infty$, where subscript ∞ refers to the ambient value), u_j is the jth component of the velocity vector, and $u_n = u_i\,n_i$. Note that the effect of viscous stresses has been neglected. Two formulations are used in this report (section 3.4): in the original formulation (Ffowcs Williams & Hawkings 1969), ρ is the density. A second formulation based on pressure is used (Spalart & Shur 2009). In the absence of volume integral, the only difference with the original formulation is that $\rho = \rho_\infty + p'/{c_\infty}^2$, where ρ_∞ is the ambient density.

F_1 and F_2 and then windowed (see section 3.2) after subtracting the mean and time-Fourier-transformed. The time derivative of F_1 is calculated in the frequency space. The retarded time ($exp(-i\omega r/c_\infty)$) is also applied in the frequency space. The integral of the source terms over the surface then yields the Fourier transform of the pressure at the observer location (with the Fourier transform of g, $\hat{g}(\omega) = \int_{-\infty}^{\infty} g(t)e^{-i\omega t}dt$):

$$4\pi\hat{p}(\mathbf{x},\omega) = \int_S i\omega\,\hat{F}_1(\mathbf{y},\omega)exp(-i\omega r/c_\infty)d\mathbf{y} + \int_S \hat{F}_2(\mathbf{y},\omega)exp(-i\omega r/c_\infty)d\mathbf{y}. \tag{2.2}$$

The Narrowband Sound Pressure Level (SPL) level (in dB) is calculated as:

$$SPL(\mathbf{x},St) = 10\,log_{10}\left(\frac{2\,\hat{p}(\mathbf{x},\omega)\hat{p}^*(\mathbf{x},\omega)}{St_{min}\,p_{ref}^2}\right), \tag{2.3}$$

where $\hat{p}^*$ is the complex conjugate of $\hat{p}$, $p_{ref} = 20\mu Pa$ and $St = \omega\,D/2\pi\,U_j$.

The Overall Sound Pressure Level ($OASPL$, in dB) is calculated as

$$OASPL(\mathbf{x}) = 10\,log_{10}\left(\sum_{St=0}^{St_{max}} \frac{2\,\hat{p}(\mathbf{x},\omega)\hat{p}^*(\mathbf{x},\omega)}{p_{ref}^2}\right) \tag{2.4}$$

The two FWH surfaces used below are shown in Fig. 9 (section 3.6). The surfaces more or less follow the growth of the jet, their section increasing downstream. A vertical outflow disk is located downstream, at $x = 25\,D$ in Fig. 9. For $x < 0$, the surface follows the shape of the nozzle. Technically, all surfaces used are then open at the inflow, but

this has no consequence on the calculated sound. Note that in the following, we use the terms closed surface and open surface to refer to the fact that the outflow disk is included or excluded from the FWH surface (see section 3.5).

In terms of outflow disk, a third option is considered: averaging over outflow disks. This technique was first used by Shur *et al.* (2005). It consists in computing $\hat{p}$ using Eq. 2.2 for several surfaces having the exact same shape, but with the outflow disks located at different axial locations. Results in $\hat{p}$ from the different surfaces are then averaged. The spurious noise generated by the passage of turbulent eddies through the outflow disk is not consistent from one surface to another. It is thus partially or totally cancelled when doing the averaging (section 3.5). The outflow disks will be regularly spaced. The spacing between two consecutive outflow disks is denoted by Δ_{min}, and the distance between the first and the last outflow disks is denoted by Δ_{max}. When outflow disk averaging is used, the first outflow disk is always located at $x = 25\,D$, so that the set of surfaces over which averaging is performed is entirely described by Δ_{min} and Δ_{max}.

3. Results

As the focus is not on the LES themselves, only a short presentation is given. LES are performed using a compressible version of the unstructured LES solver CDP, CDP-C, developed by Shoeybi *et al.* (2009). CDP-C is a second-order finite volume solver, with a hybrid implicit-explicit time advancement scheme. Small-scale turbulence is modeled using the dynamic modeling procedure of Moin *et al.* (1991) with Lilly's modification (Lilly 1992). The artificial bulk viscosity method (see Cook & Cabot 2005) in a generalized form is used to capture shock waves on unstructured grids in CDP-C code. This model has further been improved by Mani, Larsson & Moin (2009) to minimize the effect of artificial bulk viscosity on turbulence as well as dilatational motions. In this study, the model has been adapted for unstructured grids. More details about the solver and the LES themselves are given by Shoeybi *et al.* (2009) and Mendez *et al.* (2010).

Four different large-eddy simulations will be used in this report (Table 1). Simulation S1 is an unheated perfectly expanded jet at Mach 1.4. The operating point of simulations S2, S3 and S4 is identical: a perfectly expanded heated jet is considered. The difference between the three simulations is the grid. A direct comparison will be shown in this report between S2 and S3. S4 is mainly used because different time sampling was used for this calculation (see section 3.1). For more comparisons between the three grids, the reader is referred to Mendez *et al.* (2010).

In the following, multiple options of post-processing will be tested. However, not all the used options are reminded for each test. Unless otherwise specified, the default options are the following: FWH acoustic calculations are performed using the time record specified in Table 1, and time records are windowed using the Hanning window. The sound at $100\,D$ from the nozzle exit is presented, but by default it is calculated with observers located at $50\,D$ from the nozzle exit and rescaled using the assumption that the amplitude of acoustic waves decays like the inverse of the distance from the nozzle exit (as in the experiment). The pressure-based formulation of the FWH equation is used, from data recorded over surface s01 (see Fig. 9) closed at $x = 25\,D$. Results are compared with experimental data provided by Dr Bridges (Bridges & Wernet 2008). Angles are defined from the jet axis, pointing upstream (maximum noise is observed around 150°).

Simulation	M_j	M_a	M_∞	TR	Re_j	Mesh size	$\Delta t c_\infty/R$	St_{min}	St_{max}
S1	1.4	1.4	0.008	1.0	150,000	17×10^6	0.005	0.0040	7.2
S2	1.4	1.86	0.008	1.765	76,600	17×10^6	0.005	0.0030	5.4
S3	1.4	1.86	0.008	1.765	76,600	20×10^6	0.005	0.006	5.4
S4	1.4	1.86	0.008	1.765	76,600	28×10^6	0.005	0.0031	5.4

TABLE 1. Operating conditions and numerical characteristics of the simulations performed. Subscripts j and ∞ refer to the jet at the nozzle exit and the ambient free-stream, respectively. Notations are the following: $M_j = U_j/c_j$, $M_a = U_j/c_\infty$, $M_\infty = U_\infty/c_\infty$, $TR = T_j/T_\infty$, $Re_j = \rho_j U_j D / \mu_j$ (μ_j is the dynamic viscosity at the nozzle exit), and $\Delta t c_\infty/R$ is the time step. St_{min} and St_{max} are the default values of Strouhal number used in the plots displayed.

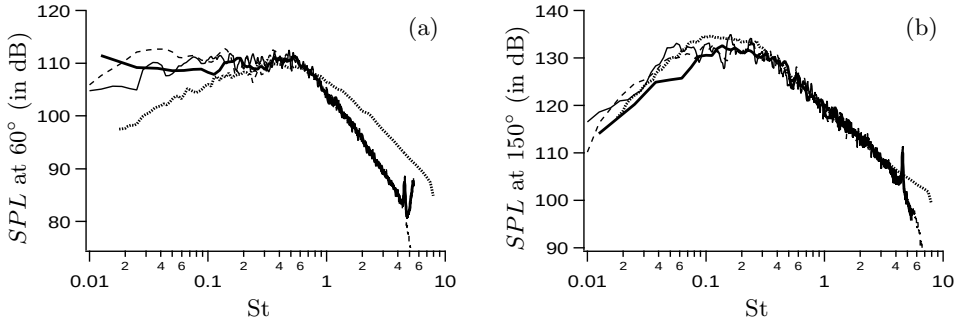

FIGURE 1. Sound pressure level at 60° (a) and 150° (b) for simulation S4 calculated with three different time records: $0.0062 < St < 10.8$ (– – – –), $0.0031 < St < 5.4$ (———), and $0.0124 < St < 5.4$ (▬▬▬). Experimental results are also displayed (▪▪▪▪▪▪▪).

3.1. *Time sampling and length of time record*

First, the influence of the time record used is shown. Two parameters are considered, the time sampling and the length of the time record, determining the maximum and minimum Strouhal numbers available for acoustic post-processing. Sound spectra for case S4 are shown in Fig. 1. Concerning the time sampling, it is shown that aliasing is visible at upstream angles when $St_{max} = 5.4$ (thin and thick solid lines in Fig. 1). When sampling frequency is doubled, results differ at high frequencies (Fig.1a). This is not observed for downstream angles. In the calculations presented here, aliasing is visible for upstream angles only, and for frequencies that do not seem well resolved by the current numerical setup. The time sampling is then considered sufficient and does not alter meaningful results.

The length of the time record is also varied in Fig. 1 to test the convergence at low frequencies. It is shown that spectra depart from a more converged spectrum if $St < 10\,St_{min}$: at a given St, results are converged if 10 periods have been accumulated.

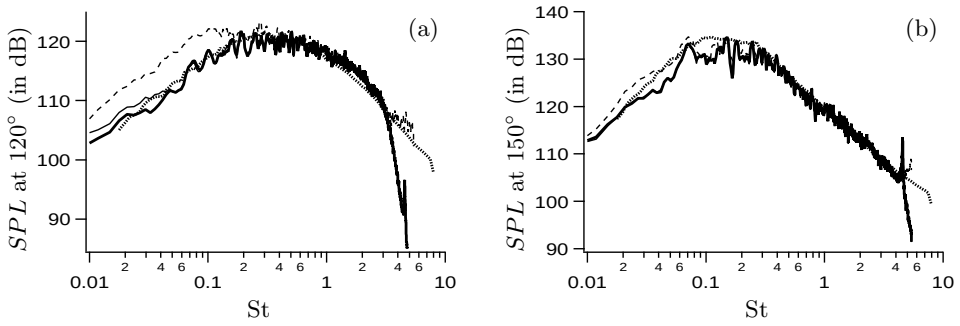

FIGURE 2. Sound pressure level at 120° (a) and 150° (b) for simulation S2 calculated with three different windowing procedures: no windowing (– – – –), hyperbolic tangent windowing (———), and Hanning windowing (▬▬▬). Experimental results are also displayed (▪▪▪▪▪▪▪).

3.2. *Windowing*

To avoid spectral leakage, signals are windowed before post-processing. Figure 2 compares results without windowing, results using a hyperbolic tangent (HT) type window, or using a Hanning window. Window functions using hyperbolic tangent have been used before to maximize the time record effectively taken into account (Freund 2001; Ham *et al.* 2009). Sound spectra presented in Fig. 2 show that windowing is necessary. HT and Hanning windows give very similar results, except at low frequencies, where Hanning window gives slightly lower sound. However, the range of frequencies where HT and Hanning windowed results differ is the range where results are not fully converged. In the following, Hanning window is systematically used.

3.3. *Observer distance*

In the formulation of the FWH equation employed here, no far-field assumption has been made. Acoustic results thus depend on the distance of the observer to the nozzle exit. This dependance is addressed by computing the acoustic far-field at different observer distances and rescaling them using the r^{-1} decay of acoustic waves to obtain the acoustic far-field at $100\,D$. Note that experimental results are obtained by measuring the acoustic field at $50\,D$ and projecting it to $100\,D$.

Figure 3 shows the acoustic far-field at $100\,D$. Overall sound pressure level is presented rescaling results calculated at $50\,D$ (as in the experiment), $100\,D$, and $125\,D$. It can be seen that $50\,D$ is not sufficient to be in the region where acoustic waves decay as r^{-1}. On the contrary, results calculated at $100\,D$ and $125\,D$ are very close. A consequence of this figure is that results will be calculated at $50\,D$ and rescaled to match the experimental procedure. This also shows that a far-field assumption can change the results.

3.4. *Formulation of the FWH equation*

Spalart & Shur (2009) have shown that the original FWH formulation is inferior to another formulation using pressure instead of density fluctuations (see section 2). They argue that the density formulation is not well suited to situations where important entropy fluctuations cross the FWH surface. In that case, density fluctuations ρ' significantly differ from their acoustic estimation from pressure fluctuations: p'/c^2. Spalart & Shur (2009) show that volumetric terms (quadrupoles) in the FWH equations are more compact when computed in the pressure formulation. As a consequence, the error made by neglecting their effect outside the FWH surface is lower in the pressure formulation. Us-

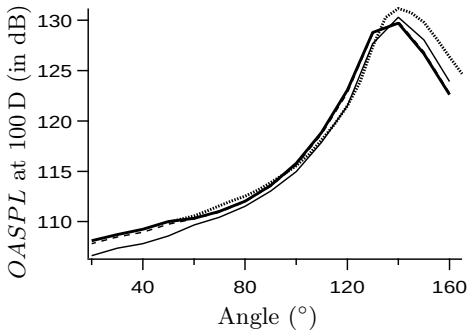

FIGURE 3. Overall sound pressure level for simulation S2 calculated at three different observer distances, $50\,D$ (———), $100\,D$ (– – – –), and $125\,D$ (▬▬), and rescaled at $100\,D$. Experimental results are also displayed (▪▪▪▪▪▪▪). They are calculated at $50\,D$ and rescaled.

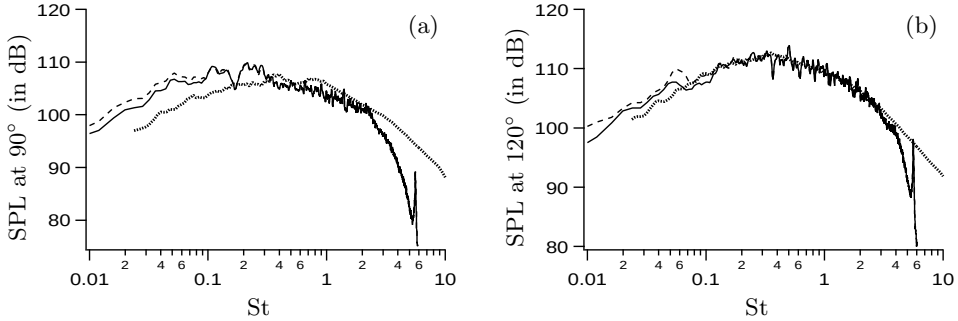

FIGURE 4. Sound pressure level at 90° (a) and 120° (b) for simulation S1 (unheated) calculated with the density formulation (– – – –) and the pressure formulation (———). The outflow disk of the FWH surface is located $27.5\,D$ from the nozzle exit. Experimental results are also displayed (▪▪▪▪▪▪▪).

ing a pressure-based formulation is thus expected to improve results, particularly for hot jets. As observations on FWH results differ depending on authors, tests were performed to verify the conclusions from Spalart & Shur (2009).

Density and pressure formulations were first compared in the case of an unheated jet, the outflow disk of the FWH surface being included (Fig. 4). Sound spectra were almost identical, consistently with expected low entropy fluctuations.

The same observation was made for heated jets when the outflow disk was excluded from the computation (not shown). Vortical motions only rarely cross the surface, as it is located apart from the jet and open at the downstream end. Differences between ρ' and p'/c^2 are small, so results from the density and the pressure formulations were almost identical.

Figure 5 shows sound spectra for the heated simulation S2, calculated using a FWH surface with the outflow disk located $25\,D$ downstream of the nozzle exit. In this case, improvement from the use of the pressure form of the FWH equation is substantial. The over-prediction at low frequencies is significantly reduced, especially at downstream angles. Improvement is probably limited to low frequencies due to the grid stretching in the axial direction: the grid cannot sustain high-wavenumber waves, thus limiting the frequency content at the end of the FWH surface to low frequencies.

In conclusion, based on our experience, the pressure-based formulation is better than

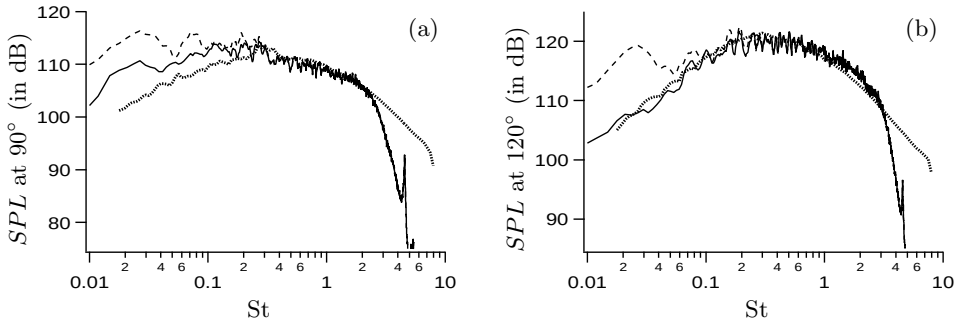

FIGURE 5. Sound pressure level at 90° (a) and 120° (b) for simulation S2 calculated with the density formulation (– – – –) and the pressure formulation (———). The outflow disk of the FWH surface is located 25 D downstream of the nozzle exit. Experimental results are also displayed (▪▪▪▪▪▪▪).

the original density formulation. All the results obtained in this study are consistent with the results shown by Spalart & Shur (2009).

3.5. *Outflow disk*

All studies using the FWH equation to compute the sound generated by high-speed jets have debated the question of the outflow disk. Articles often concluded that open surfaces yield better results than closed surfaces (among them Rahier *et al.* 2003; Uzun *et al.* 2004; Eastwood *et al.* 2009). They stated that vortical motions crossing the surface create strong unphysical noise. On the contrary, Shur *et al.* (2005) showed results where the open surface provides highly inaccurate predictions at low frequencies. Moreover, they argued that using open surfaces leads to a loss of information at shallow angles, close to the downstream axis. From the results they obtained, closed surfaces are superior to open surfaces. Note that Shur *et al.* (2005) also used 'outflow disk averaging', explained in section 2. Results were substantially improved, in particular at upstream angles, where the amplitude of the physical noise is not sufficient to mask the spurious noise related to the outflow disk. This summary shows that the question of the outflow disk is complex and obviously depends on the implementation, as results differ depending on authors. As a consequence, it is essential to test the different options with the implementation chosen here.

Note first that results using closed surfaces with the outflow disk at different distances from the nozzle exit (25 D, 27.5 D, 30 D, 32.5 D) have been compared, without observing major differences. Turbulent eddies do cross the outflow disks of all these surfaces, but the spurious noise is similar for all surfaces. Of course, this conclusion would be different if the outflow disks were too close to the nozzle exit.

Figure 6 compares the sound spectra obtained from simulation S1 with a closed surface with the outflow disk at $x = 30\,D$, an open surface (the same without outflow disk), and averaging the results from 11 surfaces with their outflow disks located between $x = 25\,D$ and $x = 30\,D$ ($\Delta_{max} = 5.0\,D$) and spaced by $\Delta_{min} = 0.5\,D$. Note first that the effect of the closure is limited to low frequencies ($St < 0.3$), which depends directly on the grid resolution at the outflow disk location. For both angles considered, results using outflow disk averaging are more accurate. In particular, the experimental shape is recovered. Closed surface results are much noisier at low frequencies for the station located at 60° (Fig. 6a), while they are close to the averaged results at 120° (Fig. 6b). At 60° (Fig. 6a),

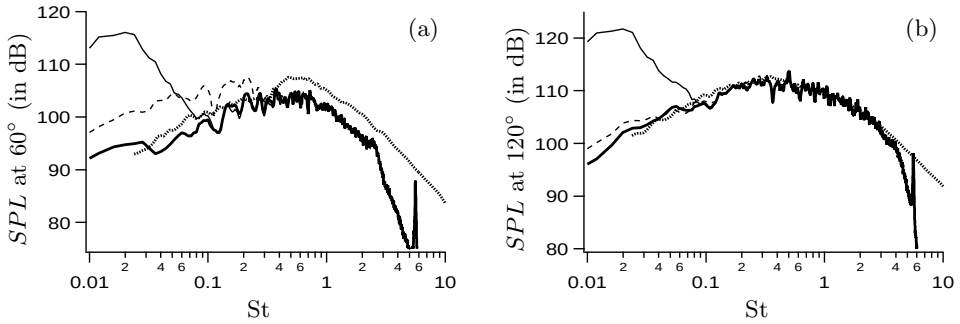

FIGURE 6. Sound pressure level at 60° (a) and 120° (b) for simulation S1 (unheated) changing the outflow disk closure: surface with outflow disk at $x = 30\,D$ (– – – –), same surface without outflow disk (———), and results averaged using 11 surfaces with $\Delta_{min} = 0.5\,D$ and $\Delta_{max} = 5.0\,D$ (▬▬). Experimental results are also displayed (▪▪▪▪▪▪).

spurious results are obtained for $St < 0.3$. Results using the open surface depart from the averaged results at lower frequency ($St < 0.1$). However, the errors at low frequencies are impressive. Note that exactly the same types of errors are shown for open surfaces by Shur *et al.* (2005), who identified them as pseudo-sound generated by the passage of vortices near the downstream end of the open FWH surface.

The same test has been performed on the heated case S2 with the original formulation (not shown), with exactly the same observations. However, as discussed previously in section 3.4, the formulation has no influence when using open surfaces, whereas the spurious sound obtained using closed surfaces with the original formulation is higher than with the pressure formulation. Note also that outflow disk averaging is not sufficient to completely correct these errors.

Finally, the same comparison is shown for simulation S4 using the pressure formulation, at four different angles with, again, the same conclusions (Fig. 7). Note also that among the four angles displayed in Fig. 7, only the upstream angle predictions (Fig. 7a) are really inaccurate using a closed surface. On the contrary, open surfaces show spurious artifacts at all angles.

From the results shown here, one can propose an explanation for the differences in the conclusions of previous studies regarding the effect of the outflow disk treatment:

(*a*) Using a pressure-based formulation reduces the spurious noise caused by closed surfaces. On the contrary, the formulation has no effect on open surfaces. Authors choosing to use open surfaces calculate the far-field sound with the original density-based formulation,

(*b*) Shur *et al.* (2005) show comparisons of open and closed surfaces at sideline and downstream angles, where spurious effect of closed surfaces are less visible than at upstream angles,

(*c*) In the present study, the spurious effect of closed surfaces is limited to low frequencies, because of the grid stretching. It appears that studies in favor of open surfaces generally use an axial grid stretching that is either less aggressive than in the present study and in Shur *et al.* (2005) or no stretching at all (see for example Rahier *et al.* 2003; Uzun *et al.* 2004). In the latter cases, outflow disk errors contaminate all the spectra and are much more noticeable.

However, it is not clear why all studies do not show important errors resulting from pseudo-sound at low frequencies using open surfaces. Nevertheless, best results are ob-

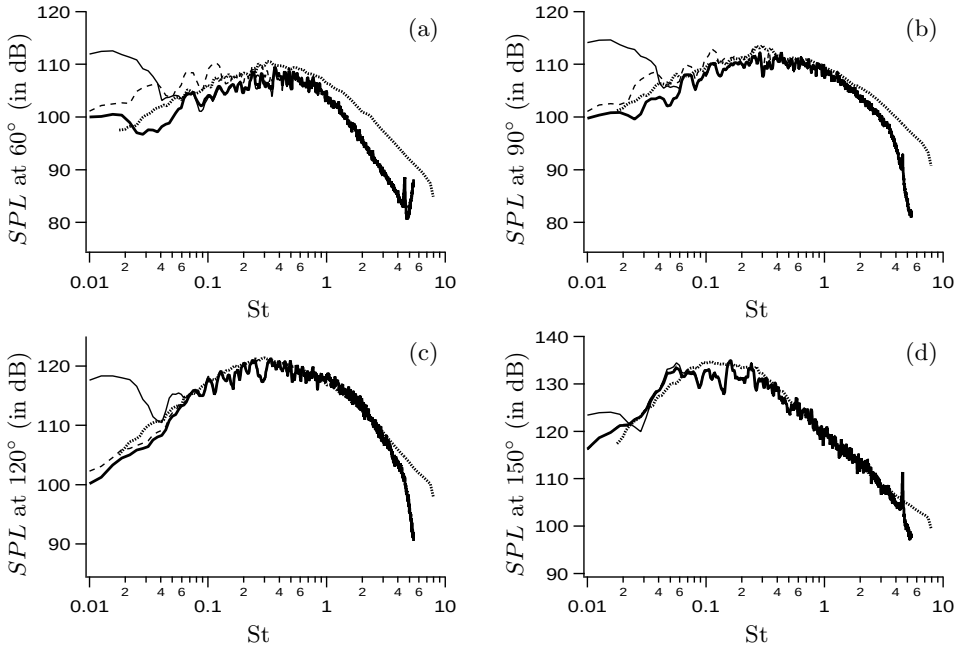

FIGURE 7. Sound pressure level at 60° (a), 90° (b), 120° (c) and 150° (d) for simulation S4 (heated) changing the outflow disk closure, using the FWH pressure formulation: surface with outflow disk at $x = 25\,D$ (– – – –), same surface without outflow disk (———) and results averaged using 11 surfaces with $\Delta_{min} = 0.5\,D$ and $\Delta_{max} = 5.0\,D$ (▬▬▬). Experimental results are also displayed (▪▪▪▪▪▪▪).

tained using outflow disk averaging. However, additional parameters are involved when outflow disk averaging is used. The following figures aim at clarifying how to chose the number of surfaces for averaging, and the distance between their outflow disks.

A simple reasoning is used to estimate St_s, the Strouhal number for which outflow disk averaging has maximum effect. Let us consider that the passage of a vortex at time t through an outflow disk is seen by an observer as a spurious acoustic wave that we consider sinusoidal, of period t_s. If this vortex is frozen and convected at the convection speed U_c, it reaches a second outflow disk with the time delay Δ/U_c, where Δ is the streamwise distance between the outflow disks of the two surfaces. When reaching the second outflow disk, the frozen vortex will produce the same sinusoidal spurious wave. Using a far-field hypothesis, the two spurious signals are seen by a far-field observer shifted by the same time delay, Δ/U_c. In this case, pure cancellation of the two signals occurs if $\Delta/U_c = t_s/2$ or $St_s = U_c\,D/2U_j\,\Delta$. The relevance of this expression is addressed in the following.

Figure 8 shows how sound spectra obtained by outflow disk averaging vary by changing the distance between two consecutive outflow disks Δ_{min} (Fig. 8a) or the distance between the first and the last outflow disks Δ_{max} (Fig. 8b). An upstream angle (60°) is shown, where the effect of averaging is maximum. In Fig. 8(a), outflow disks are separated by $\Delta_{min} = 0.5\,D$, $1.0\,D$, and $2.0\,D$. The first two cases are compared: averaging with $\Delta_{min} = 0.5\,D$ or $\Delta_{min} = 1.0\,D$ gives very close results, except in the range $0.15 < St < 0.3$. If time-averaged velocity is considered as a good estimate for U_c, then $U_c \approx 0.3U_j$ in S1 in the region where outflow disks are located. With $\Delta_{min} = 0.5\,D$,

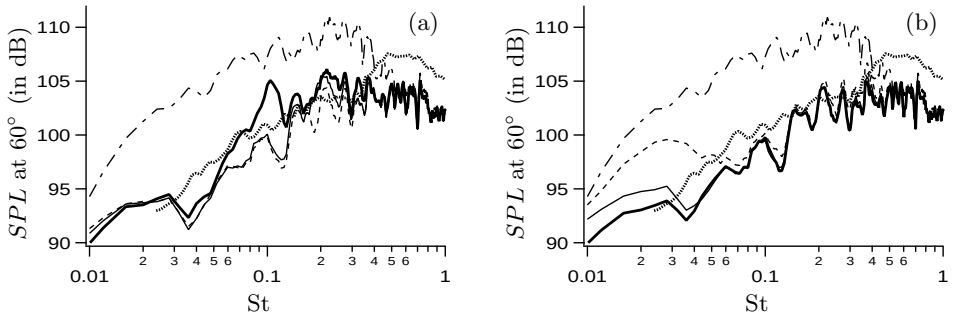

FIGURE 8. Sound pressure level at 60° for simulation S1 (unheated) calculated using outflow disk averaging. (a) $\Delta_{max} = 6.0\,D$ (– – – –), $\Delta_{min} = 0.5\,D$ (– – – –), $\Delta_{min} = 1.0\,D$ (———) and $\Delta_{min} = 2.0\,D$ (▬▬▬). (b) $\Delta_{min} = 0.5\,D$ and $\Delta_{max} = 2.5\,D$ (– – – –), $\Delta_{max} = 5.0\,D$ (———) and $\Delta_{max} = 7.5\,D$ (▬▬▬). Results from a closed surface with the outflow disk at $x = 25\,D$ (— – —) is shown for a. and b. Experimental results are also displayed (▪▪▪▪▪▪▪).

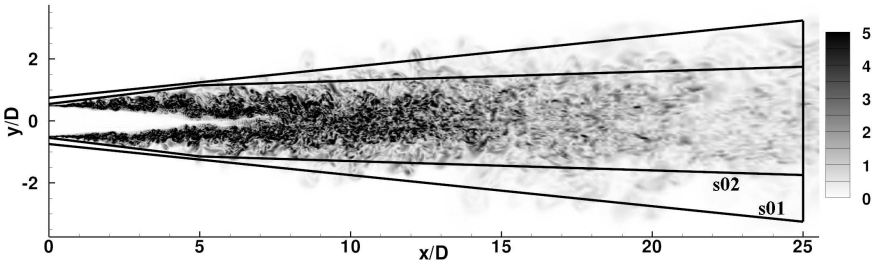

FIGURE 9. Vorticity magnitude (non-dimensionalized by c_∞/R) in an instantaneous solution from case S2. Surfaces s01 (loose) and s02 (tight) are shown. The nozzle (not shown) is located between $x = -7.55\,D$ and $x = 0$.

the maximum effect for outflow disk averaging should be seen for $St_s = 0.3$. The simple formula used above gives a good approximation, although high, of the range of maximum effect of averaging. This is also confirmed by comparing the cases where $\Delta_{min} = 1.0\,D$ and $\Delta_{min} = 2.0\,D$. Maximum efficiency for $\Delta_{min} = 1.0\,D$ should be seen around $St_s = 0.15$, and the two cases indeed differ in the range $0.06 < St < 0.15$.

Figure 8(b) shows how results obtained by averaging vary by changing Δ_{max}. When using outflow disk averaging, Δ_{max} appears to determine the low-frequency limit of effectiveness of averaging. Spurious effects are moved down to lower and lower frequencies as Δ_{max} increases. Three cases are compared: $\Delta_{max} = 2.5\,D$ ($St_s = 0.06$), $\Delta_{max} = 5.0\,D$ ($St_s = 0.03$), and $\Delta_{max} = 7.5\,D$ ($St_s = 0.02$). Again, the relevance of the formula to evaluate St_s is observed. It is shown in Fig. 8(b) that averaging over surfaces with $\Delta_{max} = 5.0\,D$ (resp. $7.5\,D$) mainly reduces the spurious sound around $St = 0.03$ (resp. $St = 0.02$) compared to the case where $\Delta_{max} = 2.5\,D$ (resp. $5.0\,D$).

3.6. *Surface location*

The question of the surface location is of particular importance when stretched grids are used. Figure 9 shows the location of surfaces s01 and s02, used in Fig. 10, together with an instantaneous field of vorticity magnitude (case S2). Both surfaces (but especially s02) are placed very close to the jet and are regularly crossed by vortices. Surfaces s01 and s02 are closed, with their outflow disk located at $x = 25\,D$.

Figure 10 shows how sound predictions can be modified by the surface location (solid

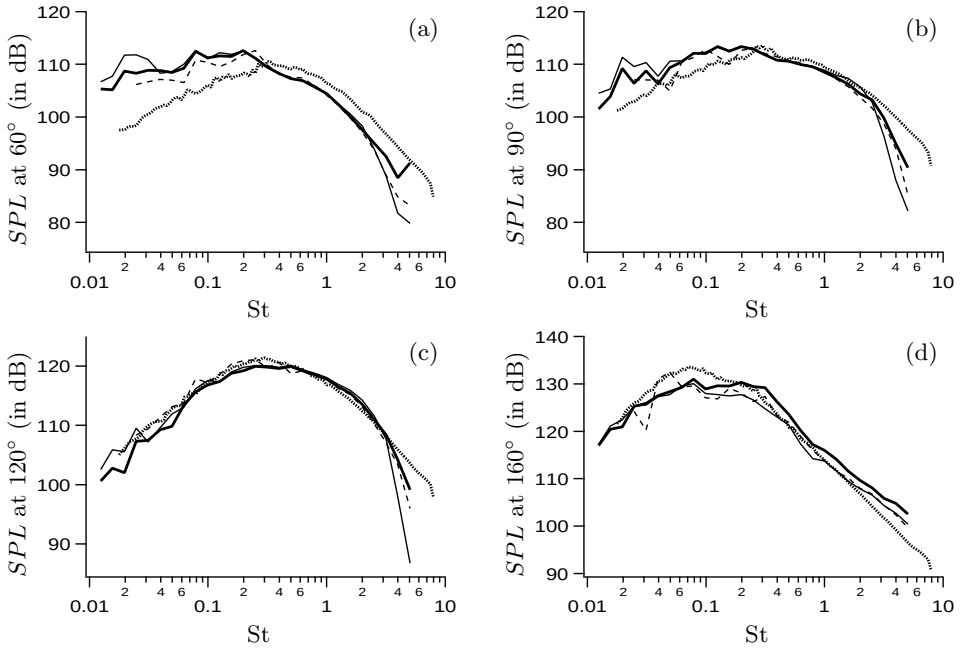

FIGURE 10. Sound pressure level, averaged over 1/3rd octave, at 60° (a), 90° (b), 120° (c), and 160° (d) calculated for simulation S3 using surface s01 (see Fig. 9) (– – – –) and for simulation S2 using s01 (——) and s02 (▬▬), compared to experimental measurements (▪▪▪▪▪▪▪).

lines). To be able to distinguish the results accurately, SPL have been bin-averaged over 1/3rd octave for this figure. A third set of numerical results (discussed below) is also shown (dashed lines). Several observations can be made on the comparison of the noise results using either s01 or s02 to post-process simulation S2. Note first that at low frequencies, the sound is lower using s02, because of a too small radial extension of the surface for large distances from the nozzle: part of the sound at low frequencies is generated outside s02. This sound is then missed by the FWH calculation, which omits the volume integration.

Another unwanted consequence of using s02 can be observed in Fig. 10(d). At this shallow angle, the sound predicted using s02 is generally 3 dB higher than using s01. This is obviously spurious, as the difference in the grid refinement cannot explain this over-estimation. Surface s02 actually crosses the source region too much, as shown in Fig. 11. The root mean square of the quadrupole term of the FWH equation (integrand of the volume integration) is displayed: $\frac{\partial^2 T_{ij}}{\partial x_i \partial x_j}$, where $T_{ij} = \rho u_i u_j + (p' - {c_\infty}^2 \rho')\delta_{ij}$. Note that, as classically done, viscous stresses are ignored in this expression of T_{ij}. Ideally, one would use a FWH formulation without volume integral only if this term is zero outside the surface. From Fig. 11, it can be seen that surface s02 cuts the source zone quite severely in the region $1\,D < x < 2\,D$. In additional tests (not shown), shifting the surface slightly away from the jet in this zone has significantly decreased the spurious noise at shallow downstream angles.

A striking difference between surfaces s01 and s02 is for high frequencies. For all angles considered, using s02 leads to higher sound at high frequencies, recovering values closer to experimental ones. Using a tight surface also decreases the spurious trend at high

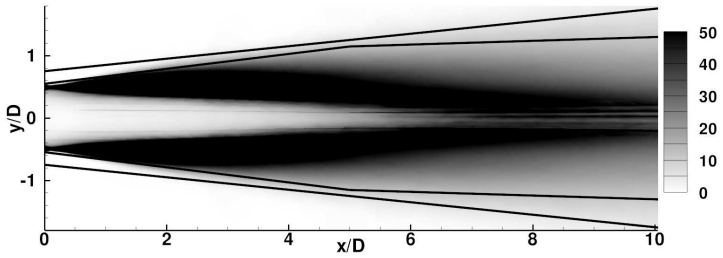

FIGURE 11. Cutting plane $z = 0$ showing the root mean square of the quadrupole term in the FWH equation (double divergence of the Lighthill tensor T_{ij}), non-dimensionalized by $\rho_\infty {c_\infty}^2/R^2$. Results are azimuthally averaged except in the core, where the grid is unstructured.

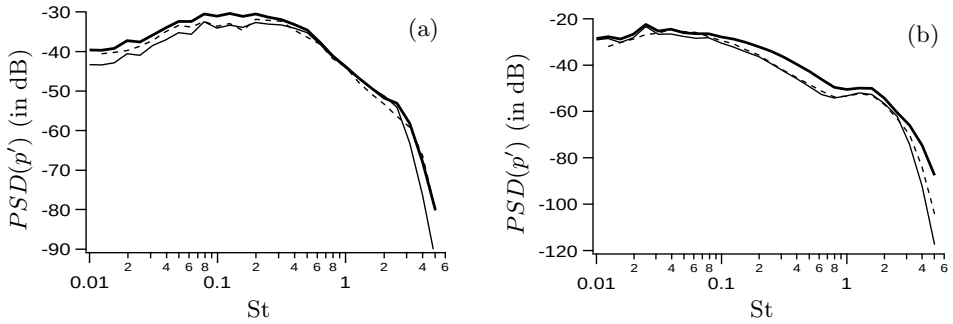

FIGURE 12. Power spectral density (PSD) of pressure fluctuations, in dB (the reference pressure is p_∞) at $x = 5\,D$ (a) and $x = 15\,D$ (b), on the surfaces used to calculate the sound in Fig. 10: simulation S3, surface s01 (– – – –) and simulation S2, surfaces s01 (———) and s02 (▬▬). Experimental results are also displayed (▪▪▪▪▪▪▪).

frequency, which results in a violent drop in the intensity of the noise, preceded by a small bump, as observed for example in Fig. 10(b) for $St \approx 1.5$ using surface s01. This is directly related to the grid resolution. The grid along surface s02 is finer than along s01. Surface s02 thus supports higher wavelengths. This is confirmed by comparing power spectral density of pressure fluctuations along the two surfaces (Fig. 12). At $x = 5\,D$ and $x = 15\,D$, pressure from the simulation is extracted at the location of surfaces s01 and s02 and spectra are displayed. Figure. 12(a) has to be compared with the view of the grid used in S2 (Fig. 13a). As the grid is stretched in the radial direction, the grid cutoff wavelength is smaller for s01 than for s02, resulting in a drop in turbulent fluctuations for smaller values of the Strouhal number (Fig. 12a). This has direct consequences on the far-field noise.

This shows the importance of the grid resolution in the high Mach number flows considered here. In order to make the sound calculation less sensitive to the surface location, a new grid has been used for simulation S3. The difference between cases S2 and S3 lies only in the radial grid refinement in the intermediate region between the main noise sources and the surface location (see Fig. 13). By improving the radial grid resolution for acoustic propagation, one can increase the grid cutoff wavelength at the location of surface s01(Fig. 12) and recover better sound predictions without moving the surface, as shown in Fig. 10.

Note that improvement in sound predictions thanks to better radial resolution is not the same for all angles. At upstream angles (Fig. 10a), the refinement is obviously not

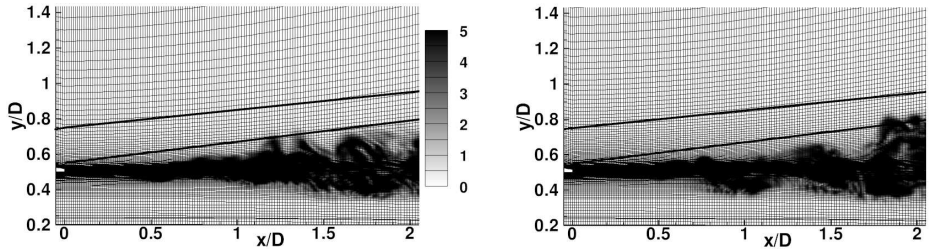

FIGURE 13. Cutting plane $z = 0$ showing the grid and vorticity magnitude (non-dimensionalized by c_∞/R) near the nozzle exit in instantaneous solutions from cases S2 (left) and S3 (right). Surfaces s01 (loose) and s02 (tight) are shown, as in Fig. 9.

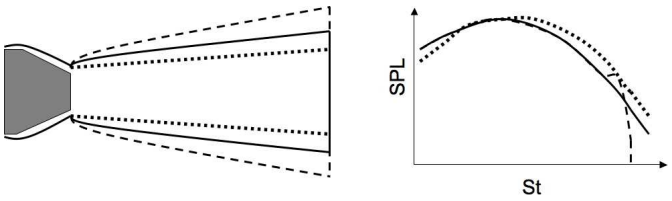

FIGURE 14. Schematic of the influence of the surface location on the sound calculated in the far-field. The solid line represents the optimal surface. The dotted-line surface cuts the jet severely while the dashed line displays a surface too far from the jet, in a zone where the grid is coarsened.

sufficient to improve significantly the results. On the contrary, predictions at 90° and 120° are significantly better at high frequencies for case S3 than for case S2, using the same surface s01. Results remain unchanged at shallow downstream angles, where no drop is observed for case S2.

As a conclusion on the surface location, it is obvious that the surface should be located as close as possible from the jet when stretched grids are used. However, defining a simple and universal criterion is difficult. In order to make the results less sensitive to the surface location, the grid has to be designed with particular care in the region where the acoustic waves propagate before reaching the FWH surface.

Even if the location where the surface should be placed is difficult to determine, trends in terms of the change in the results with the surface location can be easily defined (see Fig. 14). A hypothetical optimal surface location is considered. Using a surface away from this location will make the sound at high frequencies drop, the cutoff frequency associated with the grid being lower away from the jet, caused by grid stretching. For frequencies just lower than the cutoff frequency, increase of the noise will be seen: under-resolved fluctuations are artificially dispersed to lower frequencies. Using a radially too tight surface will produce two types of spurious effects:

(a) The surface is too tight far from the nozzle exit. A loss of information can occur, observed in particular at low frequencies. Far from the nozzle exit, sound sources associated with low frequencies have a large radial extension. Sound deficit at low frequencies caused by too tight surface has been observed for all angles (Fig. 10).

(b) The surface is too tight near the nozzle exit and crosses the zone of intense sources. In our calculations, this spurious effect has been seen for very shallow downstream angles and for a wide range of frequencies (Fig. 10(d) when surface s02 is used). It contaminates other angles when the surface crosses the jet even more aggressively. An interesting

feature is that the radial gradient of noise sources is high in the first few diameters of the jet. This permits having a surface very close to the jet axis without crossing the jet.

4. Conclusions and future work

This work focused on the post-processing of LES of supersonic jets for the extraction of acoustic far field. The FWH integration, with omission of the volume integral, has been used for this purpose. It should allow for optimal use of the FWH solver developed for the jet noise project for the future calculations.

A set of best practices can be deduced from this study:

(*a*) The pressure-based formulation is better than the original density-based formulation for FWH predictions with omission of the volume integral. Improvement is observed in terms of spurious noise through the use of FWH surfaces cutting the noise source region (typically at the outflow disk).

(*b*) In conjunction with the FWH equation based on pressure, closed surfaces give better results than open surfaces. However, spurious noise is still visible for upstream observers. The use of outflow disk averaging significantly decreases this spurious noise and should be used routinely. The combination of pressure-based formulation and outflow disk averaging provides the best results.

(*c*) The study of outflow disk averaging has shown that the number and the spacing of the outflow disks can be estimated from a simple expression, given in this report.

(*d*) Classical windowing should be used; the Hanning window is used here.

(*e*) To obtain converged acoustic results at a given period, the time record used for FWH computations has to be at least 10 times longer.

(*f*) Since the experimental results available here are probably not measured in the far field, the far-field assumption is not used. Note that the running time that could be saved using a far-field assumption is not considered significant, as the main time-consuming step of the calculations is the LES.

(*g*) The FWH surface can be intermittently crossed by the edge of the jet without generating noticeable spurious noise. However, no clear criterion has been determined to define the optimal location of the FWH surface. To make noise results less sensitive to the FWH surface location, the grid has to be designed with care, to ensure the proper propagation of acoustic waves from the location where they are generated to the surface.

Acknowledgments

This study is funded by NASA in the framework of the NASA Research Opportunities in Aeronautics. Dr. J. Bridges and Dr. J. De Bonis, NASA Glenn Research Center, are gratefully acknowledged for their help and for sharing the experimental database.

REFERENCES

Bodony, D. J. & Lele, S. K. 2008 Current status of jet noise predictions using large-eddy simulation. *AIAA Journal* **46** (3), 364–380.

Bogey, C. & Bailly, C. 2006 Investigation of downstream and sideline subsonic jet noise using large eddy simulation. *Theoret. Comput. Fluid Dynamics* **20** (1), 23–40.

Bridges, J. & Wernet, M. P. 2008 Turbulence associated with broadband shock noise in hot jets, AIAA 2008-2834. In *14th AIAA/CEAS Aeroacoustics Conference, Vancouver, CANADA, 5-7 May 2008*.

Cook, A. W. & Cabot, W. H. 2005 Hyperviscosity for shock-turbulence interactions. *J. Comput. Phys.* **203**, 379–385.

Eastwood, S., Tucker, P. & Xia, H. 2009 High-performance computing in jet aerodynamics. In *Parallel Scientific Computing and Optimization* (ed. S. N. York), *Springer Optimization and Its Applications*, vol. 27, pp. 193–206.

Farassat, F. & Myers, M. K. 1988 Extension of Kirchhoff's formula to radiation from moving surfaces. *J. Sound Vib.* **123** (3), 451–460.

Ffowcs Williams, J. E. & Hawkings, D. L. 1969 Sound generation by turbulence and surface in arbitrary motion. *Phil. Trans. R. Soc. Lond.* **264**, 321–342.

Freund, J. B. 2001 Noise sources in a low-Reynolds-number turbulent jet at Mach 0.9. *J. Fluid Mech.* **438**, 277–305.

Ham, F. E., Sharma, A., Shoeybi, M., Lele, S. K. & Moin, P. 2009 Noise prediction from cold high-speed turbulent jets using large-eddy simulation. AIAA 2009-9. In *47th AIAA Aerospace Sciences Meeting Including The New Horizons Forum and Aerospace Exposition, Orlando, Florida, 5-8 January 2009*.

Lighthill, M. J. 1952 On sound generated aerodynamically : I. General theory. *Proc. R. Soc. Lond. A* **211**, 564–581.

Lilly, D. K. 1992 A proposed modification of the Germano sub-grid closure method. *Phys. FluidsA* **4** (3), 633–635.

Mani, A., Larsson, J. & Moin, P. 2009 Suitability of artificial bulk viscosity for large-eddy simulation of turbulent flows with shocks. *J. Comput. Phys.* **228** (19), 7368–7374.

Mendez, S., Shoeybi, M., Sharma, A., Ham, F. E., Lele, S. K. & Moin, P. 2010 Large-eddy simulations of perfectly-expanded supersonic jets: Quality assessment and validation. AIAA 2010-271. In *48th AIAA Aerospace Sciences Meeting Including The New Horizons Forum and Aerospace Exposition, Orlando, Florida, 4-7 January 2010*.

Moin, P., Squires, K., Cabot, W. & Lee, S. 1991 A dynamic subgrid-scale model for compressible turbulence and scalar transport. *Phys. FluidsA* **3** (11), 2746–2757.

Rahier, G., Prieur, J., Vuillot, F., Lupoglazoff, N. & Biancherin, A. 2003 Investigation of integral surface formulations for acoustic predictions of hot jets starting from unsteady aerodynamic simulations. AIAA 2003-3164. In *9th AIAA/CEAS Aeroacoustics Conference, Hilton Head, South Carolina, May 12-14, 2003*.

Shoeybi, M., Svärd, M., Ham, F. & Moin, P. 2009 An adaptive hybrid implicit-explicit scheme for DNS and LES of compressible flows. *Submitted to J. Comput. Phys.* .

Shur, M. L., Spalart, P. R. & Strelets, M. K. 2005 Noise prediction for increasingly complex jets. Part I: Methods and tests. *Int. J. Aeroacous.* **4** (3&4), 213–246.

Spalart, P. R. & Shur, M. L. 2009 Variants of the Ffowcs Williams–Hawkings equation and their coupling with simulations of hot jets. *Int. J. Aeroacous.* **8** (5), 477–492.

Tam, C. K. W. 1995 Supersonic jet noise. *Annu. Rev. Fluid Mech.* **27**, 17–43.

Tam, C. K. W. 1998 Jet noise: since 1952. *Theoret. Comput. Fluid Dynamics* **10**, 393–405.

Uzun, A., Lyrintsis, A. S. & Blaisdell, G. A. 2004 Coupling of integral acoustics methods with LES for jet noise prediction. *Int. J. Aeroacous.* **3** (4), 297–346.